Adrenergic receptor antagonism induces neuroprotection and facilitates recovery from acute ischemic stroke

Hiromu Monai[a,b,1], Xiaowen Wang[a], Kazuko Yahagi[a], Nanhong Lou[c], Humberto Mestre[c], Qiwu Xu[c], Yoichiro Abe[d], Masato Yasui[d], Youichi Iwai[a], Maiken Nedergaard[c,e], and Hajime Hirase[a,e,f,1]

[a]Laboratory for Neuron-Glia Circuitry, RIKEN Center for Brain Science, 351-0198 Wako, Saitama, Japan; [b]Faculty of Core Research Natural Science Division, Ochanomizu University, 112-8610 Tokyo, Japan; [c]Center for Translational Neuromedicine, University of Rochester Medical Center, Rochester, NY 14642; [d]Department of Pharmacology, School of Medicine, Keio University, 160-8582 Tokyo, Japan; [e]Center for Translational Neuromedicine, Faculty of Health and Medical Sciences, University of Copenhagen, 2200 Copenhagen, Denmark; and [f]Brain and Body System Science Institute, Saitama University, 338-8570 Saitama, Japan

Edited by Terrence J. Sejnowski, Salk Institute for Biological Studies, La Jolla, CA, and approved April 17, 2019 (received for review October 9, 2018)

Spontaneous waves of cortical spreading depolarization (CSD) are induced in the setting of acute focal ischemia. CSD is linked to a sharp increase of extracellular K^+ that induces a long-lasting suppression of neural activity. Furthermore, CSD induces secondary irreversible damage in the ischemic brain, suggesting that K^+ homeostasis might constitute a therapeutic strategy in ischemic stroke. Here we report that adrenergic receptor (AdR) antagonism accelerates normalization of extracellular K^+, resulting in faster recovery of neural activity after photothrombotic stroke. Remarkably, systemic adrenergic blockade before or after stroke facilitated functional motor recovery and reduced infarct volume, paralleling the preservation of the water channel aquaporin-4 in astrocytes. Our observations suggest that AdR blockers promote cerebrospinal fluid exchange and rapid extracellular K^+ clearance, representing a potent potential intervention for acute stroke.

photothrombotic stroke | adrenergic receptor | extracellular potassium ion | aquaporin-4 | AQP4

The ionic composition of the intracellular and extracellular environments in the central nervous system critically influences neuronal networks since action potentials and synaptic input rely on transmembrane electrochemical gradients. Acute stroke disrupts the ion homeostasis in the involving infarct and induces repeated spontaneous waves of cortical spreading depolarization (CSD) in patients (1, 2) and in experimental stroke models (3–5). CSD is initiated as a slowly propagating wave of depolarization that travels across the cortical surface with a velocity of ∼4 mm/min (6). Increases in extracellular potassium (K^+) and glutamate are mediators of CSD (7–10). During the peak of CSD, the extracellular potassium concentration $[K^+]_e$ rises from a basal level of 3.5–4.5 to 30–60 mM. This massive rise of $[K^+]_e$ depolarizes neurons and astrocytes, resulting in the release of neurotransmitters and the opening of voltage-dependent K^+ channels and *N*-methyl-D-aspartate receptors (NMDARs, K^+-permeable glutamate receptors), which in a positive feedforward trigger an autoregenerative elevation of $[K^+]_e$ as CSD propagates across the cortex (11). The membrane depolarization inactivates voltage-dependent Na^+ channels, resulting in prolonged electrical silence of neurons. Neurons will gradually regain responsiveness during the recovery period concurrently with normalization of ionic gradients including that of $[K^+]_e$. However, the factors determining $[K^+]_e$ recovery are poorly understood, in part because there have been few attempts to monitor cortex-wide network activity linked to CSD following stroke incidents.

Astrocytes, a major glial cell type, play a key role in the uptake of K^+ and the maintenance of ionic homeostasis through Na^+-K^+ pumps (12) and K^+ channels (13). Additionally, K^+ uptake is regulated by astrocytic Ca^{2+} signaling (14). In experimental animal models, the focal application of high K^+ on the cortical surface reliably evokes CSD (7). While the mechanisms for initiation and propagation of CSD have been investigated in the past, the recovery phase and the basis of its molecular control have received relatively little attention. Propagation of high-K^+–induced CSD in and of itself has been suggested to be benign to cortical tissue (15), or even beneficial, as it promotes development of ischemic tolerance (16). However, it is clear that spontaneously evoked waves of CSD in the setting of acute stroke enhance permanent cortical damage and compromise functional recovery (17–19).

The glymphatic model proposes that extracellular fluid movement in the brain is regulated by aquaporin-4 (AQP4), the water channel expressed predominantly in astrocytes, and by noradrenaline levels (20, 21). We found that a systemic adrenergic receptor (AdR) blockade facilitates the normalization of $[K^+]_e$ after acute ischemic stroke, improves motor recovery, and mitigates the resultant tissue damage. To test if AQP4 plays a role in this treatment mechanism, we evaluated the expression of AQP4 at various time points after stroke by histology and immunoblot. We found that AQP4 expression decreased in peripheral areas of the photothrombosis induction site, whereas pretreatment of the AdR blockers preserved AQP4 expressions after stroke. This result suggests that the positive effect of AdR blockade on the enhancement of recovery from the stroke could

Significance

Stroke is one of the most prevalent types of acute brain injury, and rehabilitation poses globally a significant personal as well as socioeconomic burden. We here demonstrate a potent mitigation of stroke-induced brain damage by blocking adrenergic receptors. Stroke induces cortical spreading depolarizations which repeatedly increases extracellular potassium. We show that adrenergic receptor antagonism promotes the normalization of extracellular medium following stroke. From a translational standpoint, this approach may offer an affordable approach to current treatments such as tissue plasminogen activator administration and mechanical thrombectomy.

Author contributions: H. Monai, Y.A., M.Y., Y.I., M.N., and H.H. designed research; H. Monai, X.W., K.Y., N.L., H. Mestre, Q.X., Y.A., and M.Y. performed research; H. Monai contributed new reagents/analytic tools; H. Monai, X.W., and H.H. analyzed data; and H. Monai, Y.A., M.Y., Y.I., M.N., and H.H. wrote the paper.

Conflict of interest statement: A patent has been applied for in Japan for adrenergic blocker treatment for stroke (H.H., H. Monai, Y.I.).

This article is a PNAS Direct Submission.

[1]To whom correspondence may be addressed. Email: monai.hiromu@ocha.ac.jp or hirase@sund.ku.dk.

This article contains supporting information online at www.pnas.org/lookup/suppl/doi:10.1073/pnas.1817347116/-/DCSupplemental.

Published online May 16, 2019.

be due to AQP4-dependent clearance of the extracellular fluid and that AdR blockers constitute a potent therapeutic alternative for the treatment of acute ischemic stroke.

Results

Adrenergic Antagonism Limits Ischemia-Induced Cortical Damage. To investigate if AdR blockade is an effective treatment against ischemic injury, we employed a photothrombotic stroke model using Rose bengal to induce focal ischemia in the somatosensory cortex (*SI Appendix*, *SI Materials and Methods*). For AdR blockade, mice were pretreated with intraperitoneal administration of prazosin (10 mg/kg), atipamezole (10 mg/kg), propranolol (10 mg/kg), antagonizing alpha-1, alpha-2, and beta AdRs, respectively. We quantified tissue infarct size by 2,3,5-triphenyltetrazolium chloride (TTC) staining 24 h after photothrombosis (Fig. 1 *A*–*F*). As shown in Fig. 1 *A* and *B*, the surface infarct area, measured from TTC-stained whole brains, was significantly reduced by AdR-blocker pretreatment (13.21 ± 1.74 mm^2 vs. 5.95 ± 1.75 mm^2, $P = 0.011$). Furthermore, the infarct volume with edema compensation was also smaller in mice treated with AdR blockers (Fig. 1 *C* and *D*, 24.62 ± 4.26 mm^3 vs. 12.09 ± 2.51 mm^3, $P = 0.026$). Since there was a strong positive correlation between surface infarct area and total volume (Fig. 1*E*, $R = 0.88$, after unit dimension matching), we hereafter use infarct area as a proxy for total stroke damage. Next, we examined the contribution of specific AdR blockers alone and in combination with the inhibition of infarct development. We found that alpha-1 (prazosin) and beta (propranolol) antagonists significantly reduced the infarct area, whereas alpha-2 antagonism (atipamezole) was without significant effect (Fig. 1*F*, prazosin: $P = 0.0003$; propranolol: $P = 0.0001$; no interaction was found: $P = 0.74$, three-way ANOVA, $n = 6, 5, 7, 6, 6$, and 5 mice, respectively).

To evaluate remedial effects of the AdR-blocker treatment, we next evaluated the size of infarct in mice that received AdR-blocker treatment at increasing times after photothrombotic stroke. Remarkably, 1 or 2 h post stroke administration of AdR blockers was similarly effective in suppressing infarct development. The effectiveness of AdR antagonist treatment was lost when administered 3 h or more after the infarct (Fig. 1*G*).

Since photothrombotic ischemic lesions differ from the conventional middle cerebral artery occlusion (MCAO) model (22), we also assessed the effect of AdR blockers on ischemic injury induced by a 45-min occlusion of the MCA with a filament. TTC

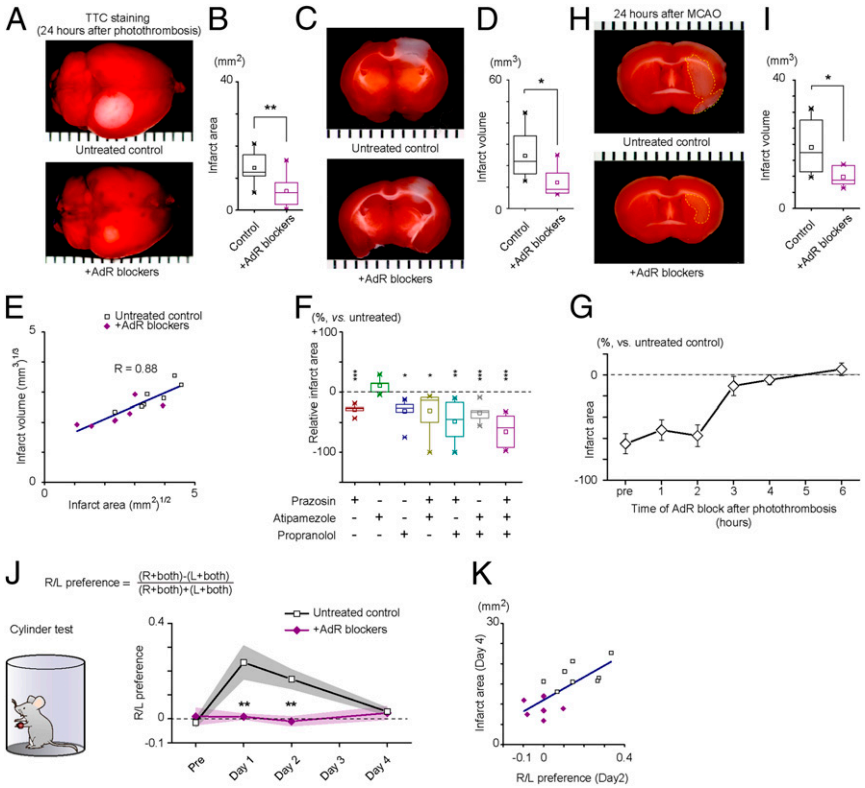

Fig. 1. Mitigation of infarction by AdR blockade. (*A*) Evaluation of infarct area on the surface of the brain induced by photothrombosis. Whole-brain TTC staining was performed on an untreated brain (*Upper*) and an AdR-blocker–treated brain (*Lower*). (*B*) Distribution and comparison of surface infarct area (13.21 ± 1.74 mm^2 vs. 5.95 ± 1.75 mm^2, $P = 0.011$, Student's *t* test, $n = 8$ for each group). (*C*) Evaluation of photothrombosis-induced infarct with TTC staining of coronal sections. (*D*) Distribution and comparison of infarct volume (24.62 ± 4.26 mm^3 vs. 12.09 ± 2.51 mm^3, after edema volume compensation, $P = 0.026$, Student's *t* test, $n = 7$ for each group). (*E*) Scatter plot showing the relationship between infarct area and infarct volume after unit dimension matching. Results of untreated control (open squares) and AdR-blocker pretreatment (purple diamonds) experiments are plotted. A high correlation coefficient of $R = 0.88$ is calculated. (*F*) Comparison of effect on the infarct area size with combinations of AdR blockers. Treatments with prazosin or propranolol showed significant effects (prazosin: $P = 0.0003$; propranolol: $P = 0.0001$; no interaction was found: $P = 0.74$, three-way ANOVA, $n = 6, 5, 7, 6, 6$, and 5 mice, respectively; post hoc Tukey–Kramer test vs. control: prazosin—$P = 0.00029$; propranolol—$P = 0.012$; prazosin + atipamezole—$P = 0.019$; prazosin + propranolol—$P = 0.0012$; atipamezole + propranolol—$P = 0.00084$). (*G*) Relative infarct size is plotted against the timing of AdR-blocker administration. AdR-blocker treatment is no longer effective when administered 3 h or longer after photothrombosis. Infarct area was evaluated by TTC staining and normalized to the mean infarct area of untreated controls. (*H*) Evaluation of MCAO-induced infarct with TTC-stained sections. (*I*) Distribution and comparison of infarct volume ($n = 6$ each, 19.09 ± 8.70 mm^3 vs. 3.11 ± 1.27 mm^3, $P = 0.03$, Student's *t* test). (*J*) Evaluation of lateralized (R/L) limb usage preference by the cylinder test. (*K*) Correlation between infarct area and limb usage laterality. For *A*, *C*, and *H*, ticks represent 1-mm spacing. $*P < 0.05$, $**P < 0.01$, and $***P < 0.001$.

staining of brain sections after 24 h showed that AdR-blocker administration 30 min before MCAO was effective in decreasing infarct volume (Fig. 1 *H* and *I*, 19.09 ± 3.55 mm^3 vs. 9.78 ± 1.27 mm^3, $P = 0.03$). Collectively, these results indicate that AdR blockers are neuroprotective in two well-established murine ischemic stroke models.

Milder Focal Ischemia-Induced Motor Dysfunction After Adrenergic Antagonism. Given that somatosensory and motor cortices are functionally and anatomically associated, we evaluated the effect of AdR blockers on ischemic damage by quantifying motor function with the cylinder test, whereby the laterality of preferred limb usage is assessed in a mouse exposed in a hollow cylinder (23) (Fig. 1*J*). We found that mice with stroke showed a higher lateral bias in the usage of forelimb. Stroked mice favored the usage of the ipsilateral forelimb on day 1 and day 2 compared with prestroke (day 0) forelimb usage [right/left (R/L) preference; 0.24 ± 0.07 vs. 0.17 ± 0.04, day 0 vs. day 2, $P = 0.037$], whereas no such bias was observed in the AdR-blocker pretreated group (0.01 ± 0.01 vs. −0.01 ± 0.02, day 0 vs. day 2, $P = 0.35$). Next, we assessed the relationship between forelimb usage laterality and infarct area. The analysis identified a strong positive correlation between forelimb usage laterality (day 2) and infarct area (day 4) (Fig. 1*K*, $R = 0.52$), The scatter plot (Fig. 1*K*) shows that the AdR-blocker treatment reduced the infarct size and forelimb usage laterality. In addition, we longitudinally monitored the open field locomotor activity of stroked mice. Consistent with the forelimb usage observations, locomotor activity recovered in 9 d for mice without treatment, whereas mice treated at either 30 min before, or up to 2 h after, stroke recovered in 4 d (*SI Appendix*, Fig. S1).

Adrenergic Antagonism Reduces Asynchronous Aberrant Astrocytic Ca^{2+} Activities After Photothrombosis. To gain insight into the changes occurring in cortical cellular activity by photothrombotic stroke, we monitored the Ca^{2+} dynamics of neurons and astrocytes in layer 2/3 of the somatosensory cortex (1 mm away from the ischemic core) by two-photon microscopy. We expressed jRGECO1a and G-CaMP7 in cortical neurons and astrocytes, respectively, by AAV1-Syn.NES-jRGECO1a.WPRE.SV40 and AAV9-hGFAP-G-CaMP7. After a 20-min photothrombosis induction, aberrant astrocytic Ca^{2+} activities appeared for ∼20 min in anesthetized untreated mice (Fig. 2*A*). These aberrant astrocytic Ca^{2+} activities were not synchronous, except for the passage

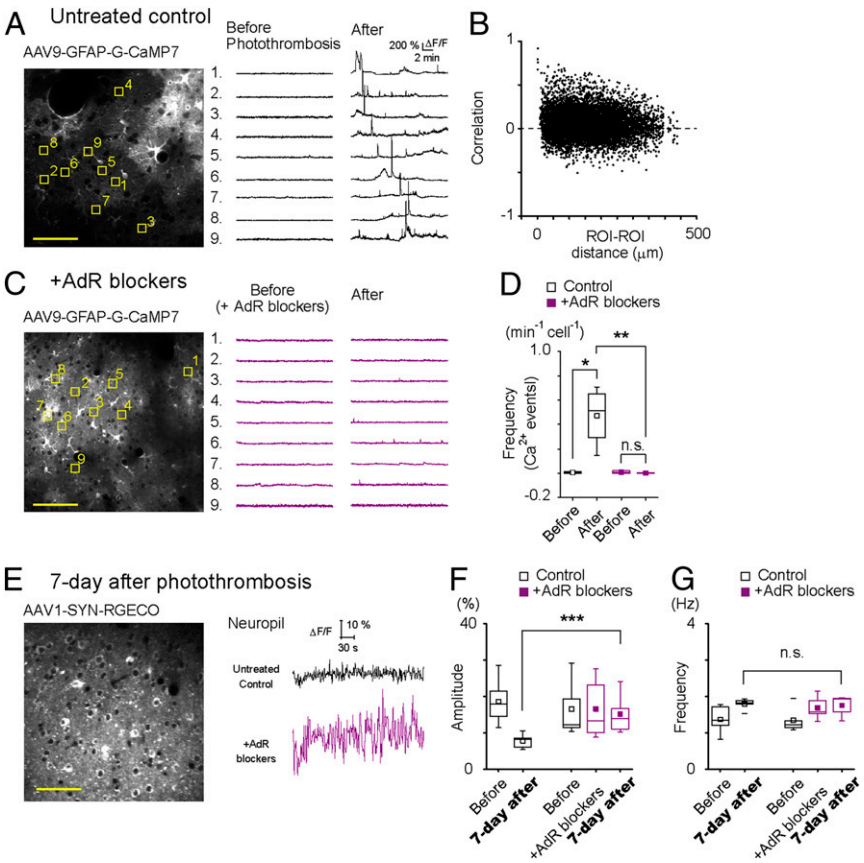

Fig. 2. AdR antagonism reduced asynchronous aberrant astrocytic Ca^{2+} activity after photothrombosis and improved neuronal activity recovery on day 7. (*A–E*) Spontaneous astrocytic Ca^{2+} activities were monitored with G-CaMP7 before and after photothrombosis to evaluate the effect of AdR-blocker pretreatment. Images are taken from somatosensory cortex layer 2/3 (1 mm away from the ischemic core). (*A*, *Left*) A sample image of G-CaMP7 expressed in astrocytes. Nine representative gliopil regions were chosen (yellow squares), and their Ca^{2+} activities are plotted on the *Right*. Aberrant astrocytic Ca^{2+} activities are observed after photothrombosis. (*B*) A large majority of postphotothrombotic gliopil Ca^{2+} activities had near-zero pairwise correlation coefficients (166 ROIs from four mice). (*C*) AdR-blocker pretreatment (prazosin, atipamezole, and propranolol) suppresses the aberrant astrocytic Ca^{2+} elevations after photothrombosis. (*D*) Mean frequency of astrocytic Ca^{2+} events 20 min after photothrombosis. (*E–G*) Neuronal Ca^{2+} activities were monitored by RGECO1a at 7 d after photothrombosis. (*E*, *Left*) Representative image of layer 2/3 somatosensory cortex with neuronal RGECO expression. (*E*, *Right*) Sample traces of neuropil spontaneous Ca^{2+} activity. (*F*) Mean amplitude of spontaneous neuropil activities is plotted for untreated mice and AdR-blocker–treated mice before and 7 d after photothrombosis. (*G*) Mean frequency of spontaneous neuropil Ca^{2+} activities. $^*P < 0.05$, $^{**}P < 0.01$, $^{***}P < 0.001$, and not significant (n.s.), $P > 0.05$. (Scale bar, 50 μm.)

of spreading depression waves, and had a sporadic occurrence as evidenced by the majority of correlation coefficients of Ca^{2+} activity between pairs of gliopils were close to zero (Fig. 2*B*). AdR-blocker pretreatment with diminished photothrombosis-induced aberrant astrocytic Ca^{2+} activity (Fig. 2*C*). AdR antagonism significantly reduced the frequency of aberrant Ca^{2+} events after photothrombosis [Fig. 2*D*, Ca^{2+} event frequency ($min^{-1}cell^{-1}$): before vs. after, untreated control: 0.0071 ± 0.0095 vs. 0.47 ± 0.24, $P = 0.035$; AdR blockers: 0.011 ± 0.013 vs. 0.0024 ± 0.0057, $P = 0.40$]. Of note, neuronal Ca^{2+} activity in the penumbral region was hardly detectable except for the passage of spreading depression waves during the 20-min period following photothrombosis induction.

Long-Term Effect of Adrenergic Antagonism. Given the accelerated motor recovery of AdR-blocker–treated mice after photothrombosis, we sought to examine the functional dynamics of the peri-infarct area in the more chronic state. Therefore, we imaged neuronal Ca^{2+} activity 7 d after photothrombosis (Fig. 2*E*). The mean amplitude of spontaneous Ca^{2+} events was significantly reduced by photothrombosis (Fig. 2*F*, before vs. after; 18.64 ± 1.86 vs. 7.81 ± 0.76, $P = 1.32E\text{-}5$), whereas AdR treatment before photothrombosis resulted in comparable neuronal Ca^{2+} event amplitudes on day 7. On the other hand, the frequency of spontaneous Ca^{2+} events was similar in untreated and treated mice (Fig. 2*G*, before vs. after; 1.35 ± 0.16 vs. 1.75 ± 0.13, $P = 0.16$). Of note, AdR-blocker treatment itself did not change amplitude or frequency (Fig. 2 *F* and *G*, amplitude: before AdR treatment vs. after AdR treatment vs. after photothrombosis; 16.55 ± 3.54 vs. 16.57 ± 3.73 vs. 15.18 ± 2.50, $P = 0.94$; frequency: before AdR treatment vs. after AdR treatment vs. after photothrombosis; 1.35 ± 0.35 vs. 1.69 ± 0.16 vs. 0.285 ± 0.13, $P = 0.15$).

Next, we performed transcranial Ca^{2+} imaging of G7NG817 mice 7 d after photothrombosis. As shown in *SI Appendix*, Fig. S2*A*, photothrombotic stroke induced an area characterized by a high-intensity fluorescent signal, presumably reflecting signals from necrotic or depolarized (hence high Ca^{2+}) cells (*SI Appendix*). Indeed, the G-CaMP7 signal remained abnormally elevated with minimal fluctuations at the photothrombotic site (i.e., compromised area). Prestroke administration of AdR blockers markedly reduced the stroke area as defined by high-intensity G-CaMP7 signal, and UP/DOWN state-like slow oscillations were observed in the neuropil of penumbra areas, which is indicative of synaptic activity (24). To quantify lesion size, we computed the size of the compromised area according to the degree of Ca^{2+} signal fluctuations (*SI Appendix*, *SI Materials and Methods*). This analysis demonstrated that the compromised area was significantly reduced by AdR blockers (*SI Appendix*, Fig. S2*B*, $n = 4$ mice for both groups, 4.34 ± 1.16 mm^2 vs. 0.74 ± 0.38 mm^2, $P = 0.0044$). Furthermore, AdR blockers also accelerated the recovery of spontaneous activity at off-center photothrombosis induction areas (*SI Appendix*, Fig. S2*C*, 110.84 ± 14.90 vs. 206.95 ± 34.55 a.u., $P = 0.0077$).

To establish that improved poststroke recovery of motor function by AdR-blocker pretreatment is associated with a reduction in astrocytic inflammation in the peri-infarct regions, we performed histology 7 d after cortical photothrombosis. Immunolabeling against glial fibrillary acidic protein (GFAP) and microglia marker protein (Iba1) in horizontal sections revealed reactive changes in astrocytes extending beyond the ischemic lesion (~6 mm away from the center) and in microglia (~3 mm away from the center). We examined the intensities of GFAP and Iba1 signals in the motor cortex peri-ischemic core area (~4 mm from the infarct border; *SI Appendix*, Fig. S2*D*). The photothrombotic stroke induced significant increases in GFAP and Iba1 immunolabeling in both photothrombosis groups, but the signal was significantly lower in animals with AdR blockade (*SI Appendix*, Fig. S2*E*) (GFAP: untreated stroke vs. AdR-blocker–treated stroke vs. no-stroke control: 12,440 ± 946 vs. 9,083 ± 965 vs. 2,083 ± 165 a.u., $P = 0.02$, one-way ANOVA, $F = 42.82$). AdR blockers visibly inhibited microglial reactivity 7 d after photothrombosis as quantified by the significant reduction of Iba-1–positive area and intensity (*SI Appendix*, Fig. S2 *F* and *G*; untreated control, $n = 6$ mice vs. +AdR blockers, $n = 6$ mice, core: 3.46 ± 1.73 vs. 2.97 ± 1.84, $P = 0.55$; Peri1: 4.10 ± 1.41 vs. 2.23 ± 1.39, $P = 0.0081$; Peri2: 1.77 ± 1.23 vs. 1.32 ± 0.32, $P = 0.0014$, repeated measures one-way ANOVA).

Adrenergic Antagonism Alters the Postischemic Changes in AQP4 Expression. Since stroke injury owes largely to the formation of edema, we hypothesized that the molecular mechanisms mediating the neuroprotection by AdR blockers are related to the water dynamics of the hyperacute phase of stroke. Therefore, we investigated the changes in the brain water channel AQP4 expression in peripheral areas (~2 mm away from the infarct border). Immunohistochemistry of the peripheral area (2 mm away from the center of photothrombosis) 3 h after photothrombosis shows that the AQP4 expression is visibly decreased (Fig. 3*A*). This decline in AQP4 confirmed a previous observation in an MCAO model (25) and traumatic brain injury model (26). By contrast, the glutamate/aspartate transporter (GLAST/EAAT1) did not show obvious expression changes, also in agreement with a previous report (27). Other astrocytic membrane proteins, namely glutamate transporter-1 (GLT-1/EAAT2) and connexin 43 (CX-43), also showed visibly decreased expressions (Fig. 3*D* and *SI Appendix*, Fig. S3*A*). Interestingly, AdR-blocker pretreatment attenuated the decreases of AQP4, GLT-1, and Cx-43 expressions (Fig. 3 *B* and *D* and *SI Appendix*, Fig. S3*B*). Accordingly, we sought to investigate the time course of expression changes of these critical astrocytic proteins.

Next, we examined the time dependence of expression patterns after photothrombosis induction (Fig. 3*C*, *Upper*). Here, AQP4 expression progressively declined with time after photothrombosis to a nadir of about 40% of basal expression, whereas the GLAST expression did not show obvious changes (Fig. 3*E*). We next examined the time dependence of AdR blockers on AQP4 expression changes (Fig. 3*C*, *Lower*). As shown in Fig. 3*E*, 1-h postincident administration of AdR blockers preserved AQP4 levels. Furthermore, 2-h postincident administration spared ~70% of the AQP4 signal, which is significantly higher than 40% sparing in untreated controls. These results suggest that the AdR blockade preserved AQP4 expression [Fig. 3*E* (1), vs. Fig. 3*F* (5): 15.32 ± 2.70% vs. 9.17 ± 6.16%, $P = 0.38$ (2); vs. (6): −26.89 ± 7.00% vs. −24.72 ± 3.96%, $P = 0.79$)], which was otherwise progressively ablated after photothrombosis [(3) vs. (6): −54.34 ± 4.92% vs. −24.72 ± 3.96%, $P = 0.00085$] (numbers in parentheses refer to the numbers in Fig. 3 *E* and *F*). However, GLT-1 and CX-43 expressions were not preserved by 2-h postincident AdR blockade (*SI Appendix*, Fig. S3*B*). The notable rescue of AQP4 expression by the AdR blockade seems consistent with the recently proposed glymphatic model, which posits AQP4-dependent cerebral fluid exchange during states of low noradrenergic tonus, such as sleep (20, 21).

To confirm that the diminished AQP4 immunofluorescent signal after stroke is due to down-regulation of surface AQP4 protein, we performed Western blotting on the membrane fraction of cortex samples on the photothrombosis and contralateral sides (*SI Appendix*, Fig. S4). Here we found that the surface AQP4 protein level was unchanged in the initial hour after photothrombosis, irrespective of AdR-blocker pretreatment. However, the cell-surface AQP4 expression was decreased by about 40% at 3 h after photothrombosis, whereas AdR-blocker pretreatments tended to attenuate the degree of this down-regulation (−27.2 ± 3.2%). To test the hypothesis that cortical adrenergic receptor activation leads to the diminishment of AQP4, we applied alpha-1 and beta agonists onto the cortex through a

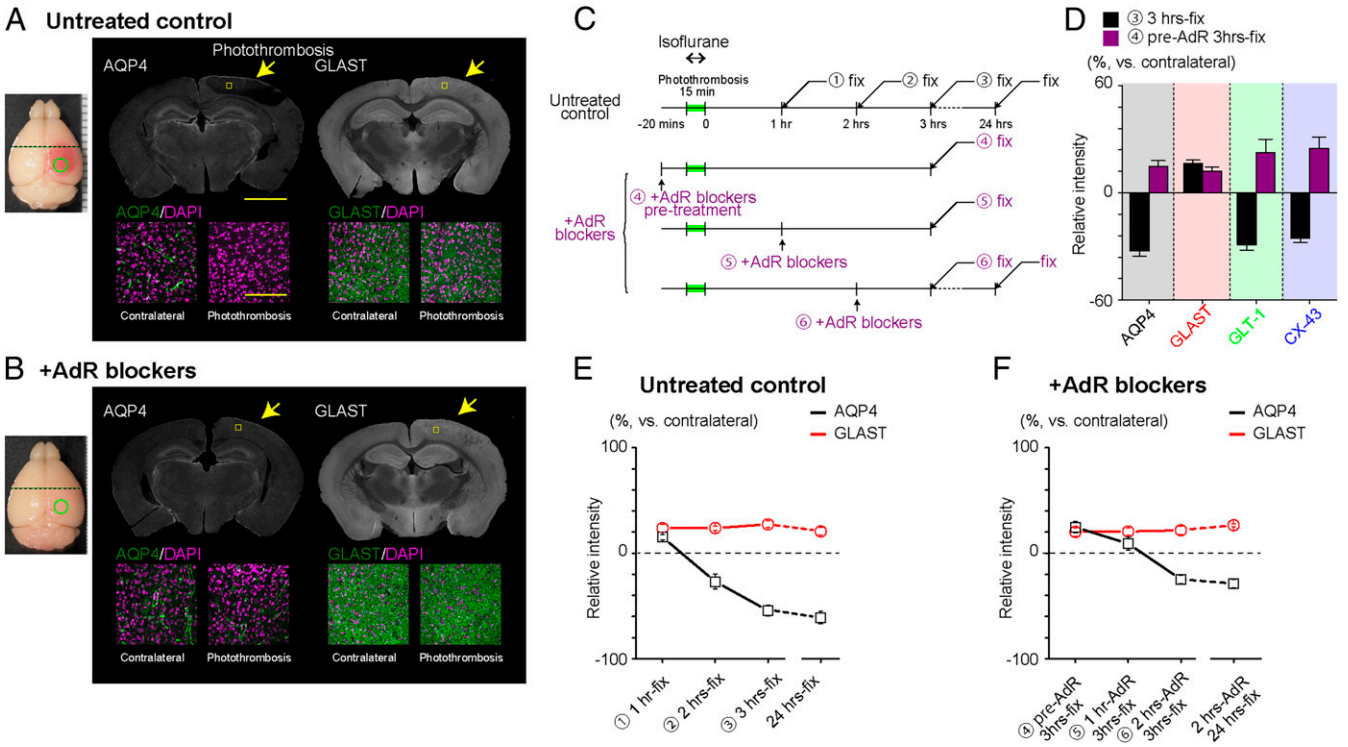

Fig. 3. AdR blockade preserves AQP4 expression in photothrombotic stroke-induced infarct areas. (*A*) Representative immunohistochemical labeling of AQP4 and GLAST 3 h after photothrombosis in an untreated mouse. Note contrasting patterns of AQP4 and GLAST expression at the peripheral area (yellow arrow). (*A*, *Bottom*) High magnification images of cortical layer 2/3 (yellow square). [Scale bars: 1 mm (*Top*), 100 μm (*Bottom*).] (*B*) Same as in *A* in a mouse pretreated with AdR blockers. (*C*) Experiment schedule for the subsequent immunohistochemical analysis of astrocytic membrane protein expression. Circled numbers correspond to data points in *E* and *F*. Mice were anesthetized by isoflurane (2%) during photothrombosis induction and by urethane (1.6 g/kg) 5–10 min before perfusion fixation. (*D*) Comparison of immunohistochemical signals for representative astrocytic membrane proteins. For AQP4, GLT-1, and Cx-43, relative expression levels on the contralateral side decreased 3 h after photothrombosis. AdR blockers attenuate the decrease of these proteins. GLAST expression was decreased by photothrombosis, and AdR blockade does not influence the expression after photothrombosis. (*E*) Photothrombosis progressively decreases immunohistochemical signals for AQP4, while a mild increase is observed for GLAST ($n = 6$ each, except AQP4 for 3-h fixed: $n = 9$). (*F*) AdR-blocker treatment preserves AQP expression and attenuates the decrease of AQP4 when administered 1 or 2 h after photothrombosis induction ($n = 6$ each).

small craniotomy. Application of either or both agonists attenuated the expression of AQP4 after 3 h (*SI Appendix*, Fig. S5).

Perivascular AQP4 Expression Is a Hallmark of Infarct Size Reduction by AdR Blockade. Given that AQP4 expression is enriched in perivascular astrocytic endfeet, we investigated the spatial expression pattern of AQP4 in the peripheral area (~2 mm away from the infarct border) within individual astrocytes 1 h after photothrombosis. AdR-blocker treatment conspicuously enhanced the expression of perivascular AQP4 in this hyperacute phase (Fig. 4*A*). Subsequently, when we confined our analysis to perivascular AQP4 expression (as defined by colocalization with CD-31, antiplatelet endothelial-cell adhesion molecule-1), the AQP4 immunofluorescence signal was ~50% higher when pretreated, whereas the neuropil AQP4 signal was unaffected by AdR-blocker pretreatment (Fig. 4*B*). We further analyzed the endfoot polarization of AQP4 expression. Perivascular polarity, defined as the ratio of the focally high perivascular signal area to the overall AQP4 immunoreactivity (28) (*SI Appendix*, *SI Materials and Methods*), was not significantly altered on the photothrombosis side in untreated control mice ($0.059 \pm 0.0067\%$ vs. 0.093 ± 0.011, $P = 0.11$). Intriguingly, AdR-blocker pretreatment increased the polarity of AQP4 expression (0.14 ± 0.014, $P = 0.00042$) on the photothrombotic site in the peripheral area (~2 mm away from the infarct border) (Fig. 4*C*).

Next, we sought to address the functional significance of AQP4 expression during the first hour after photothrombotic stroke by pharmacologically blocking AQP4 with the specific antagonist TGN-020 (29). We applied the TGN-020 intraperitoneally immediately after photothrombotic stroke induction in AdR-blocker–pretreated mice (Fig. 4*D*). Despite the pretreatment, subsequent administration of TGN-020 in the hyperacute phase resulted in an obvious expansion of infarct area 1 d after photothrombosis (Fig. 4*E*), attaining a size comparable to that in mice with neither AdR blockers nor TGN-020 treatment.

The essential role of AQP4 in the formation of poststroke edema is well established (30–32). To test the hypothesis that AQP4 preservation is the critical mediator of neuroprotection with AdR blockade, we measured photothrombosis-induced infarct size in AQP4 knockout (KO) mice (33). We found that AdR-blocker pretreatment was ineffective in mice lacking AQP4 water channels (untreated WT: 29.53 ± 1.58 mm^2, $n = 6$; AdR-blocker–treated WT: 18.74 ± 2.34 mm^2, $n = 5$ mice; untreated AQP4 KO mice: 25.35 ± 2.47 mm^2, $n = 5$ mice and AdR-blocker–treated AQP4 KO: 26.72 ± 1.22 mm^2, $n = 6$ mice, untreated WT vs. AdR-blocker–treated WT: $P = 0.003$, untreated WT vs. untreated KO: $P = 0.17$, and untreated AQP4 KO vs. AdR-blocker–treated AQP4 KO: $P = 0.61$, Fig. 4*F*). This result supports the notion that AQP4 indeed plays a central role in the neuroprotective effect of AdR blockers. Taken together, experiments in Fig. 4, *E* and *F*, suggest that enhanced polarization of perivascular AQP4 expression plays a significant role in reducing infarct size in photothrombotic strokes with AdR blockade.

Adrenergic Antagonism Facilitates CSD Recovery and K^+ Clearance. Since normalization of $[K^+]_e$ after stroke is a prerequisite for the

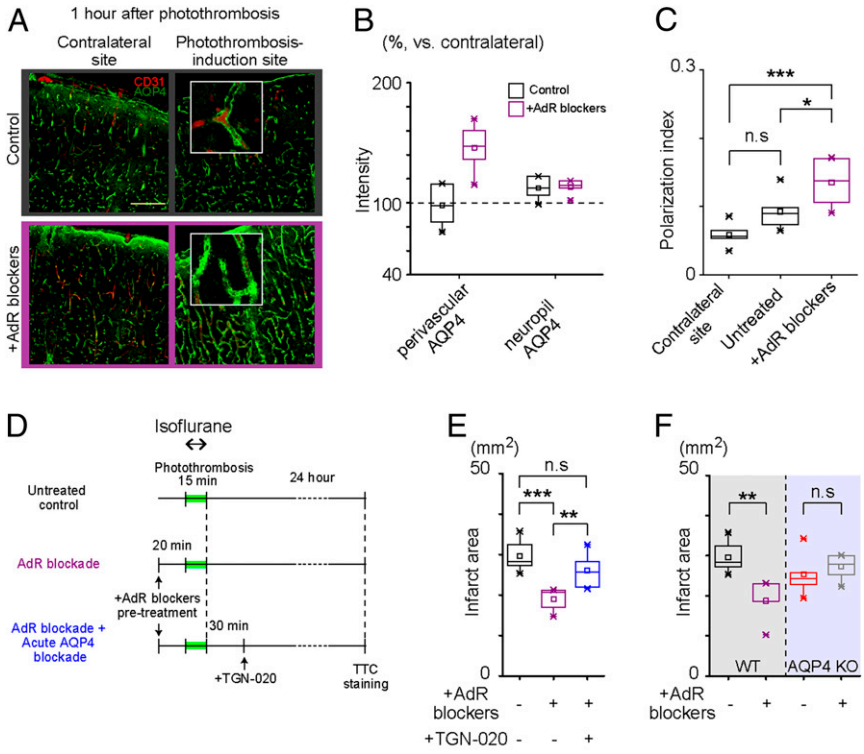

Fig. 4. Polarization of perivascular AQP4 expression is a hallmark of infarct reduction by AdR blockers. (*A*) Representative images of AQP4 expression (green) with vasculature marker (CD31, red) in the cerebral cortex 1 h after photothrombotic stroke. (Scale bar, 150 μm.) (*B*) Intensity of AQP4 immunofluorescence signal in perivascular and neuropil areas relative to the contralateral side. (*C*) Polarization index of AQP4 expression is plotted for the contralateral cortex of untreated mice and photothrombosis-induction side of untreated and AdR-blocker–pretreated mice. (*D*) Experiment schedule for the subsequent TTC staining. Mice were anesthetized by isoflurane (2%) during photothrombosis induction and 24 h later by urethane (1.6 g/kg) for 5–10 min before TTC staining. (*E*) Preemptive AdR-blocker administration does not reduce infarct size in mice that had AQP4 blocker (TGN-020) administration after photothrombosis induction. ($n = 6$ untreated + vehicle, $n = 5$ AdR blocker + vehicle, $n = 7$ AdR blockers + TGN-020). (*F*) Preemptive AdR blocker administration in AQP4 KO mice is not effective against photothrombosis-induced infarct size compared with untreated AQP4 KO mice ($n = 6$ WT, $n = 5$ WT + AdR blocker, $n = 5$ AQP4 KO, and $n = 6$ AQP4 KO + AdR blockers). $^*P < 0.05$, $^{**}P < 0.01$, $^{***}P < 0.001$, and not significant (n.s.), $P > 0.05$.

recovery of neural activity, we hypothesized that AdR blockade promotes the removal of extracellular K^+. Therefore, we recorded $[K^+]_e$ and local field potential (LFP) simultaneously in the primary somatosensory cortex (layer 2/3 of the whisker area, 2 mm away from the center of the photothrombosis site), using double-barrel K^+ electrodes in urethane-anesthetized mice (Fig. 5*A*). The baseline $[K^+]_e$ was comparable in untreated controls and AdR-blocker–treated mice (3.31 ± 0.02 vs. 3.37 ± 0.04 mM, 6 vs. 6 mice). AdR-blocker–treated mice showed significantly lower $[K^+]_e$ levels in the barrel cortex 90 min after photothrombosis induction at the somatosensory cortex, whereas high $[K^+]_e$ levels persisted for at least 3 h in the barrel cortex of control mice (Fig. 5*A*). These results show that $[K^+]_e$ normalizes faster in mice receiving AdR blockers after photothrombotic stroke. Moreover, spontaneous slow oscillation of LFP activities in the barrel cortex recovered to baseline levels with AdR-blocker pretreatment, whereas slow oscillation activity continued to be dampened 180 min after photothrombosis induction (Fig. 5*B*) without pretreatment. Remarkably, AdR blockers did not enhance K^+ clearance after photothrombosis in AQP4 KO mice, supporting a role for this water channel in K^+ normalization (Fig. 5*A*).

Given that preservation of AQP4 is critical to the effects of AdR blockers in neuroprotection, we predicted that fluid movement in the parenchyma should be affected by experimental stroke. To test this hypothesis, we infused biotinylated dextran amine (BDA; molecular weight: 70 kDa) in the cisterna magna and monitored the spread of tracer to the cerebral cortex 30 min later by developing the brain sections with fluorescence-tagged streptavidin (Fig. 5*C*). We applied this procedure 30 min after photothrombosis induction in ketamine–xylazine-anesthetized mice (intraperitoneal 70 mg/kg of ketamine and 10 mg/kg of xylazine). As expected, tracer distribution was restricted in the peripheral area (2 mm away from the center of photothrombosis). Moreover, AdR-blocker pretreatment evoked a more extensive infiltration of the tracer which resembled that in controls. The depth profile of tracer distribution in the cortex is reported in Fig. 5 *D* and *E* (control: 151.3 ± 7.2, +AdR blockers: 159.3 ± 9.7, $n = 6$, photothrombosis: 19.4 ± 20.1, photothrombosis + AdR blockers: 130.7 ± 17.4 background-subtracted arbitrary unit, $F = 15.36$, $P = 5.71E\text{-}5$, one-way ANOVA). These results suggest that AdR blockers facilitate the normalization of extracellular ion balances by replacing the high-K^+ interstitial fluid (ISF) with fresh cerebrospinal fluid (CSF) in the parenchyma.

Discussion

In this study, we report that noradrenergic antagonism reduced ischemic brain damage and accelerated motor recovery following photothrombotic stroke (Fig. 1). Moreover, AdR blockers spared the expression and polarization of AQP4, which is otherwise attenuated by photothrombotic stroke (Figs. 3 and 4). AdR blockers also facilitated normalization of $[K^+]_e$ after stroke in a manner dependent on AQP4 (Fig. 5).

The mechanism of systemic neuroprotection by adrenergic antagonism during stroke recovery likely involves a complex interaction of multiple systems and cell types. Recently, the Nedergaard group

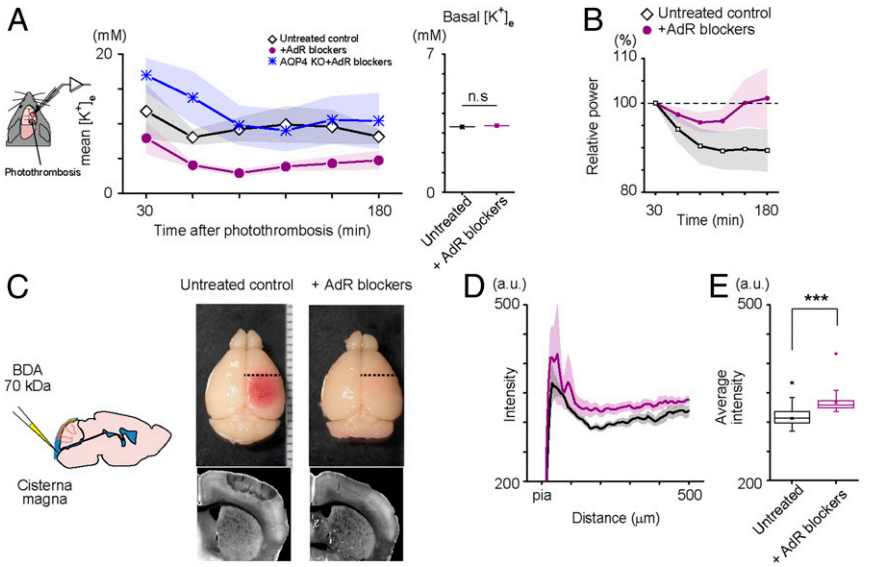

Fig. 5. AdR blockade facilitates K^+ clearance and interstitial fluid circulation. (*A*) AQP4-dependent facilitation of K^+ clearance by AdR blockers in a photothrombosis model. In vivo extracellular K^+ concentration ($[K^+]_e$) and LFP were recorded simultaneously in the somatosensory cortex 2 mm away from the center of the photothrombosis induction site. Data points are the mean values for 30-min intervals after photothrombosis. Preemptive AdR-blocker treatment does not have profound effects on basal $[K^+]_e$ or LFP; however, it facilitates K^+ clearance and LFP recovery after photothrombosis (*Right*, $n = 5$, each group). (*B*) Effect of preemptive AdR-blocker administration on the recovery of spontaneous slow oscillation activity in LFP (0.5–2 Hz) after photothrombosis. Slow oscillation LFP power is recovered faster in AdR-blocker–treated mice. ($n = 5$ vs. $n = 7$). (*C*) Evaluation of ISF circulation in the cortex. Schematic image of tracer (BDA: 70 kDa) injection to the cisterna magna with a glass pipette (*Left*). Representative images of the stained with fluorophore-tagged streptavidin distribution 30 min after injection in the fixed coronal section (*Right*). Small green circle represents the lateral center of photothrombosis. (*D*) Depth profiles of cortical fluorescent intensity. Tracer did not circulate in the peripheral area in untreated mice, but preemptive treatment with AdR blockers facilitated tracer penetration. The degree of tracer circulation is progressively enhanced with depth in AdR-blocker–treated photothrombotic mice. (*E*) Comparison of average fluorescence intensity in the analyzed area in *D* shows that preemptive AdR blockade preserves ISF clearance (Control: $n = 5$, +AdR blockers: $n = 6$, Photothrombosis: $n = 3$, Photothrombosis+AdR blockers: $n = 6$). ***$P < 0.001$, and not significant (n.s.), $P > 0.05$.

has proposed that the glymphatic system (20), a fluid exchange system between CSF and ISF, is negatively modulated by AdR activation (21). The neuroprotective effects in stroke mice seen with AdR antagonists could thus be viewed as an extension of glymphatic system function. Neurons in the locus coeruleus, the major source of noradrenergic projections to the cortex, show bursting activity during K^+-induced cortical spreading depression (34), a phenomenon observed in pathological states of the brain including ischemic stroke (18, 19).

Aberrant astrocytic activities have been reported within an hour after photothrombotic stroke (35), hinting at an active involvement of this cell type in the hyper-acute phase. Noradrenaline has been identified as one of the principal neuromodulators that trigger astrocytic Ca^{2+} activities in the cerebral cortex (36, 37). Indeed, massive noradrenaline releases by ischemic stroke have been reported in rats (38). These noradrenaline releases will activate AdRs, which in turn can restrict glymphatic flow. Blockade of AdRs would not only counteract the resultant glymphatic flow restriction, but also promote the influx of fresh CSF with normal ionic balance to the parenchyma. Such a mechanism would clear excess K^+ to the venular perivascular space. Recently, cortical $[K^+]_e$ levels were observed to be higher in awake states than in sleep, which is correlated with higher noradrenergic activity during waking (39). In support of this view, expression of AQP4, the astrocytic water channel protein critical for glymphatic flow (20), is markedly decreased 3 h after photothrombotic stroke, but was unaffected in AdR-blocker–treated mice (Fig. 3). The decrease of AQP4 after photothrombotic stroke provides additional mechanistic evidence for compromised glymphatic flow after CSD in mice (40). Indeed, tracer diffusion after injection to the cisterna magna suggested preservation of CSF/ISF flow in peripheral infarct areas by AdR blockers (Fig. 5 *C–E*). The effectiveness of AdR blockers was lost when administered 3 h after stroke, which coincided with the loss of AQP4 expression and polarity, suggesting that the main beneficial effect of AdR blockade is likely to be through preservation of AQP4.

The current literature on the role of AQP4 in ischemic stroke appears contradictory. For example, Manley et al. (30) reported improved outcomes of MCAO infarct in AQP4 KO mice, while other studies reported little effect or worse outcomes in AQP4 KO mice (41–43). In the present photothrombotic model, we found a trend ($P = 0.09$) toward reduced infarct area in AQP4 KO mice (Fig. 4*F*), agreeing with the results of Manley et al. (30). Furthermore, we find that AdR antagonism in AQP4 KO mice is ineffective in reducing infarct size, adding support for the involvement of AQP4 in stroke progression in WT mice. Meanwhile, there is a general consensus on compromised K^+ clearance in AQP4 KO mice in physiological and pathophysiological conditions, including CSD (44–46).

Considering the above, deleterious poststroke edema formation could develop in the following phases. (*i*) Hyper-acute phase: osmotic water influx through AQP4 to the parenchyma due to elevated $[K^+]_e$ contributes to swelling. (*ii*) Acute phase: astrocytic AQP4 expression decreases in an AdR-dependent manner. (*iii*) Postacute phase: water is trapped in the parenchyma, and chronic edema is established. In this model, it is conceivable that AQP4 KO (31) and pretreatment with an AQP4 blocker (29) improve outcomes of ischemia because they interfere with phase (*i*). On the other hand, AdR antagonism is effective in acute and postacute phases, when water efflux is required to mitigate against the edema formed during the hyper-acute phase. Thus, our observations can potentially explain the conflicting observation in the literature.

Enhanced recovery from CSD by AdR antagonism may also reflect modulation of cerebral blood flow (CBF). Elevation of extracellular noradrenaline levels during the post-CSD period

results in noradrenaline-dependent cerebral vessel constriction mediated by perivascular cells (47). Indeed, CBF is regulated in part by a fine balance between the alpha-1 AdR and alpha-2 AdR, which are linked to G_q and G_i signaling pathways, respectively. Since prazosin (alpha-1 AdR antagonist) can reverse the vessel constriction by atipamezole (alpha-2 AdR antagonist) (48), the AdR-blocker mixture used in this study has the net effect of reversing vasoconstriction. The AdR-blocker–induced decrease of vascular resistance would then lead to increased delivery of oxygen and glucose and possibly promote the exchange of ISF and blood, which is ultimately needed to clear K^+ from the CNS. We measured CBF using laser Doppler flowmetry. We found that the CBF decrease was less pronounced in AdR blockade mice for the first 60 min after photothrombosis under isoflurane anesthesia, suggesting that poststroke preservation of CBF may contribute to the neuroprotective effect of AdR antagonists (*SI Appendix*, Fig. S6). However, the finding that TGN-020 application failed to affect AdR blocker suggests that the enhancement of CSF/ISF exchange after AdR blockade, possibly mediated by the glymphatic system, is a favorable precondition for the recovery of neuronal activity.

Our observations show that the triple AdR-blocker combination tended to be more effective than prazosin or propranolol administered alone (both $P < 0.1$, Fig. 1*F*). Previous reports of drugs targeting alpha-2 AdRs for the treatment of ischemic brain damage have conflicting results. For example, pretreatment with alpha-2 AdR agonists is reported to be neuroprotective in some reports (49, 50), but not in others (51, 52). Moreover, postincident treatment with the alpha-2 AdR antagonist atipamezole reportedly enhanced recovery of some motor functions (53–57) even though infarct size remained similar (58). The preincident agonist approach supposedly decreases noradrenaline levels due to the presence of presynaptic alpha-2 autoreceptors (59, 60), whereas the postincident antagonist approach would increase noradrenaline levels. Our approach of using an AdR-blocker combination is distinct from previous approaches in that we antagonize a broad spectrum of AdR subtypes, thereby enhancing systemic circulation in the glymphatic and/or vascular systems. This may favor greater effects in both infarct size and motor recovery than in some previous reports.

Remarkably, we saw significant improvements in motor function recovery in AdR-blocker–treated mice exposed to somatosensory cortex ischemia. Our analysis shows that this systemic treatment can be effective in the hours after injury, suggesting a possible therapeutic potential. Of course, altered noradrenaline signaling throughout the sympathetic nervous system will interfere with autonomic body functions such as blood pressure, heart rate, and body temperature. Future preclinical studies should determine the optimal degree and nature of AdR antagonism in lissencephalic and gyrencephalic brains to minimize brain damage caused by prolonged depolarization in the setting of ischemia.

Materials and Methods

All experimental protocols were approved by The Institute of Physical and Chemical Research (Japan) (RIKEN) Institutional Animal Care and Use Committee or the University Committee on Animal Resources at the University of Rochester. Efforts were taken to minimize the number of animals used.

Surgical Procedures for Acute Experiments. Adult (older than 9 wk) male and female C57BL/6 wild type, G7NG817 (61), and AQP4-KO/GFP-KI (33) (CDB0758K, http://www2.clst.riken.jp/arg/mutant%20mice%20list.html) mice were used. G7NG817 and AQP4-KO/GFP-KI mice are available from RIKEN BioResource Center (RBRC09650 and RBRC04364, respectively). The background strain of these mice is C57BL/6. Mice were housed under a 12 h/12 h light/dark cycle and raised in groups of up to five. See *SI Appendix, SI Materials and Methods*, for details.

Drug Administration.

AdR blockers. The combination of AdR antagonists used throughout the article is as follows (except experiments for Fig. 1*F*): propranolol—10 mg/kg; prazosin—10 mg/kg; and atipamezole—1 mg/kg. These antagonists were prepared in 0.1% solution in saline and administered successively. For preemptive treatment, the drugs were applied intraperitoneally 30 min before stroke induction. For postincident treatment, drug administration was made 1–6 h after stroke induction. The control group is represented by naive mice.

TGN-020. The AQP4-specific antagonist TGN-020 (Tocris, 5425) was applied intraperitoneally immediately after photothrombotic stroke induction (Fig. 4*E* and *SI Appendix*, Fig. S6*D*; dosage: ∼500 μg/kg; 0.2 mL of 300 μM solution in saline for a 25-g mouse). See *SI Appendix, SI Materials and Methods* for details.

Photothrombosis Induction. Mice were anesthetized with isoflurane (induction: 4%; maintenance: 2%) and placed under a fluorescence stereomicroscope (Leica MZ10F). The skull was exposed via scalp incision and treated with a mixture of paraffin oil and Vaseline (1:1) to increase skull transparency. Rose bengal was administered 5 min before photothrombosis (330,000, intraperitoneal 110 mg/kg; Sigma). To induce photothrombosis, the target area (4-mm diameter, primary visual cortex) was illuminated by a green light for 15 min at the target area. See *SI Appendix, SI Materials and Methods*, for details.

MCAO. The mice were anesthetized with 1.25–3% isoflurane for induction and 0.75–1.5% for maintenance (1.25 and 0.75% were used for the AdR antagonist group to avoid morbidity during surgery; 3 and 1.5% were used for control group). The right MCA was occluded by a 7–0 polypropylene monofilament (Ethicon) coated with silicon resin, which was inserted via the external carotid artery through the internal carotid artery. Cortical blood flow was continuously monitored by laser Doppler flowmetry (Perimed). Rectal temperature was maintained at 37 ± 0.5 °C using a feedback-controlled heating system (Harvard Apparatus). Forty-five minutes after occlusion, the inserted filament was removed, and MCA blood flow was restored, as confirmed by flowmetry. The animals were returned to their temperature-controlled home cage (ThermoCare) and allowed to recover for 4 h.

Histology.

TTC staining. Twenty-four hours after photothrombosis induction, anesthetized mice were perfused with ice-cold PBS, and extracted brains were soaked in 2% TTC (Sigma) for 15 min at 37 °C. See *SI Appendix, SI Materials and Methods*, for details.

Immunohistochemistry. Mouse brains were perfusion-fixed with 4.0% paraformaldehyde (pH 7.4 in 0.1 M phosphate buffer). Following overnight postfixation in the same medium, coronal slices (60 μm thick) were prepared using a microslicer (PRO 7; Dosaka). For GFAP, AQP4, GLAST, GLT-1, and CX-43 staining, sections were incubated with primary antibodies (1:1,000 for GFAP, AQP4, GLAST, and GLT-1 antibodies and 1:2,000 for CX-43 antibody in Tris-buffered saline with 0.1% Triton X-1000) overnight. The sections were subsequently washed in phosphate buffer and incubated with Alexa 488-conjugated secondary antibodies (Invitrogen) for 2 h for fluorescent labeling. See *SI Appendix, SI Materials and Methods*, for details.

Polarization index. Double-immunolabeled fluorescent images with anti-CD31 and anti-AQP4 antibodies were used to compute polarization indices. Pixels with intensity exceeding the mean + 1 SD of the CD31 positive area were regarded as blood vessels. The AQP4 high signal area at astrocytic endfeet (Area_high) was defined by those pixels overlapping with blood vessels having AQP4 pixel intensity exceeding the mean + 1 SD of the AQP4 positive area (Area_low). CD31- and AQP4-positive areas are defined as any pixels with intensity greater than the mean of the respective image. Polarization index is defined as Area_high/Area_low.

Western Blot. Brains were removed from deeply anesthetized mice (3% isoflurane) and cortical areas of interest (surface area: ∼6 mm^2) were immediately dissected and placed separately in Eppendorf tubes (1 mL), which were then frozen in liquid nitrogen. These samples were kept in −80 °C for later Western blot analysis. See *SI Appendix, SI Materials and Methods*, for details.

Behavior Experiments.

Open field test. Individual mice were placed in an empty plastic box that had a size of 40 × 40 cm. The mice explored the box for 9 min, and the entire session was recorded. The total traveled distance was computed from the video file using MATLAB.

Cylinder test. The cylinder test was performed similarly to Li et al. (23). A transparent hollow acrylic cylinder (10 × 20 × 2 cm) was set behind two adjacently placed mirrors (26.8 × 20 cm) forming an angle of about 100°. For each test, a mouse was placed inside the cylinder for 10 min, and its behavior

was recorded by a video camera (SONY HDR-XR550V). See *SI Appendix, SI Materials and Methods*, for details.

Surgical Procedures for Virus Inoculation. pAAV-hGFAP-G-CaMP7 (a gift from Masanori Matsuzaki, University of Tokyo, Tokyo; ref. 62) was synthesized by modifying the pAAV-hSyn-EGFP vector (Addgene plasmid #50465, a gift from Bryan Roth, University of North Carolina School of Medicine, Chapel Hill, NC) with a human GFAP promoter (63) and G-CaMP7 cDNA. AAV9-hGFAP-G-CaMP7 was purified at a titer of 1.2×10^{14} vg · mL^{-1}. AAV1-Syn.NES-jRGECO1a.WPRE.SV40 (3.44×10^{13} vg · mL^{-1}) was purchased from Penn Vector Core. The viruses were diluted to 5–7 $\times 10^{12}$ vg · mL^{-1} with PBS for microinjection. Mice were anesthetized with isoflurane (1.5%) or ketamine-xylazine intraperitoneally (56 and 8 mg · kg^{-1}, respectively), and fixed in a stereotaxic frame. A small craniotomy was made at the site of prospective imaging and a glass micropipette containing AAV was inserted to a depth of 250 μm below the surface of the cortex. Microinjection of 300 nL was made over 5 min using a Femtojet injector (Eppendorf). Imaging experiments were performed at least 2 wk later.

In Vivo Two-Photon Imaging. Two-photon imaging was performed on urethane-anesthetized adult mice (as above) using a resonant-scanner–based B-Scope (Thorlabs) with a Chameleon Vision 2 laser (Coherent, wavelength 920 nm) and an Olympus objective lens (XLPlan N 25×). The B-Scope was equipped with a reverse dichroic mirror (ZT405/488/561/680–1100rpc; Chroma), and the emission light was separated by using a dichroic mirror (FF562-Di03; Semrock) with bandpass filters FF03-525/50 and FF01-607/70 (both from Semrock) for the green and red channels, respectively. Images were acquired using the ThorImage software with a frame rate of 30 Hz.

Extracellular Potassium Recording. Ion-sensitive microelectrodes for measuring extracellular K^+ were made from double-barreled glass pipettes (A-M Systems, Inc., 607000), which were pulled using a pipette puller (P-97; Sutter), and the tip was broken to have a diameter of <10 μm for each cavity. Pipettes were silanized by exposure to dimethylsilane vapor in a small container for 1 h at 200 °C. One or the other electrode tip was loaded with 2.5 μL of valinomycin-based K^+ ion-exchange resin (potassium ionophore I–mixture B, front-loaded) and subsequently filled with 150 mM KCl. The other tip was filled with 150 mM NaCl and used as a reference for the LFP recording.

K^+-sensitive electrodes were calibrated before and after each experiment using a set of solutions with known K^+ concentration (2.5, 3.5, 4.5, 10, 20, 50, 100, and 300 mM). Each electrode was calibrated by linear-regression least-squares fitting of the relationship between voltage and K^+ concentration. The offset effect by 50 μM prazosin is documented in *SI Appendix*, Fig. S7.

In vivo extracellular K^+ recordings were made using a DC amplifier (MultiClamp 700B; Axon Instruments) from cortical layer 2/3 (250 μm below the pial surface) and were recorded at a 20-kHz sampling rate. Simultaneous recordings were made from K^+-sensitive and reference LFP electrodes. The reference LFP was subtracted from the K^+-sensitive electrode recording, and the resulting data were resampled to 10 Hz and converted to millimolars according to the calibration curve.

Injection of Fluorophore-Tagged Tracer from Cisterna Magna. Neck muscles were surgically removed, and the cisterna magna membrane was carefully exposed under urethane (1.6 g/kg) anesthesia. A glass pipette (tip diameter: ~10 μm) filled with 0.5% BDA (70 kDa) in PBS was inserted into the cisterna magna by piercing the dura mater. To avoid CSF leakage, the cisterna magna membrane was immediately sealed by cyanoacrylate adhesive around the tip of the inserted glass pipet. A syringe driver (KDS Legato Series; KD Scientific) was used to infuse the fluorescence tracer at a rate of 1 μL/min for 5 min (5 μL in total). The pipette tip was left in place until the experiments were terminated at 30 min.

Recording of Physiological Parameters. Heart rate, respiratory rate, and arterial oxygen saturation level (SpO_2) were measured using a commercial pulse oximeter (MouseOx PLUS; Starr LifeSciences). In brief, the oximeter sensor was placed on a shaved area of neck above the carotid artery, and parameters were recorded in anesthetized mice (urethane, 1.7 g/kg). Laser Doppler flowmetry (Omegaflo, FLO-C1; Omegawave) was used for the measurement of CBF through the skull above the barrel area of the somatosensory cortex as previously described in Takata et al. (64)

In Vivo Transcranial Fluorescence Imaging. Mice were fixed to a stereotaxic stage by clamping the head frame and placing them under a fluorescence stereomicroscope (MZ10F; Leica). A GFP3 filter set (excitation 470 ± 20 nm, emission 525 ± 25 nm; Leica) was used with an EL6000 light source (Leica). Images were acquired using the ORCA-Flash 4.0 CMOS camera (Hamamatsu Photonics) using HC Image software (Hamamatsu Photonics). The HC Image software also controlled a shutter unit to illuminate the skull only during imaging. Images were acquired with a size of 512 × 512 pixels and 16-bit resolution. Images were acquired at 10 Hz.

Data Analysis.

Edema compensation. Edema compensation for TTC-stained coronal slices was computed according to the previously published methods (65, 66). First, we measured infarct volume including edema at the photothrombosis induction site (V_e). We next measured the volume of the entire hemisphere of photothrombosis (V_R) and finally the volume of the contralateral hemisphere (V_L). Essentially, the infarct volume compensating for edema inflation (V_i) was estimated as $V_i = V_L \times V_e/V_R$.

Correlation. For each region of interest (ROI) of gliopils, a correlation coefficient of the 1-min bin was calculated. The average of the correlations was plotted to the distance between the center of gravity of the paired ROI (Fig. 2*B*).

LFP power. LFP power for slow oscillations (Fig. 5*B*) was computed as follows: the spectrograms were calculated for LFP traces by fast Fourier transform of consecutive 10-s bins. The power of slow oscillations was then computed by averaging the amplitude of the 0.5- to 2-Hz frequency bin from the spectrogram for the period of interest.

Tracer intensity quantification. Intensity of the fluorescence tracer was quantified along the orthogonal line against the pia mater. The analyzed position was set to fall 1.5 ~ 2 mm anterior to bregma (1 mm away from the center of photothrombosis) and 2 mm from the midline. See *SI Appendix, SI Materials and Methods*, for details.

Data and Materials Availability. All transgenic mice used in this article are available from RIKEN BioResource Center.

ACKNOWLEDGMENTS. We thank Drs. Shinichi Takahashi (Keio University), Elizabeth M. C. Hillman (Columbia University), K. C. Brennan (The University of Utah), Charles Yokoyama (RIKEN), and Paul Cumming for discussion and comments on the manuscript and the RIKEN Center for Brain Science–Olympus Collaboration Center for technical assistance with image acquisition. This work was supported by the RIKEN Center for Brain Science and Japan Society for the Promotion of Science KAKENHI Grants 18K14859 (to H. Monai), 26117520, 16H01888, and 18H05150 (to H.H.), 17K19637 and 16H05134 (to Y.A.), and 15H04688 and 18H02606 (to M.Y.). This work was also supported by Human Frontier Science Program Grant RGP0036/2014 (to H.H.); Japan Society for the Promotion of Science Core-to-Core Program Advanced Research Networks; the Adelson Medical Research Foundation (M.N.); the Lundbeck Foundation; the Novo Nordisk Foundation; and the US Department of Defense (M.N.). H.H. is a recipient of the Lundbeck Foundation Visiting Professorship.

1. Mayevsky A, et al. (1996) Cortical spreading depression recorded from the human brain using a multiparametric monitoring system. *Brain Res* 740:268–274.
2. Fabricius M, et al. (2006) Cortical spreading depression and peri-infarct depolarization in acutely injured human cerebral cortex. *Brain* 129:778–790.
3. Dietrich WD, Feng Z-C, Leistra H, Watson BD, Rosenthal M (1994) Photothrombotic infarction triggers multiple episodes of cortical spreading depression in distant brain regions. *J Cereb Blood Flow Metab* 14:20–28.
4. Röther J, de Crespigny AJ, D'Arceuil H, Mosley ME (1996) MR detection of cortical spreading depression immediately after focal ischemia in the rat. *J Cereb Blood Flow Metab* 16:214–220.
5. Branston NM, Strong AJ, Symon L (1977) Extracellular potassium activity, evoked potential and tissue blood flow. Relationships during progressive ischaemia in baboon cerebral cortex. *J Neurol Sci* 32:305–321.
6. Leão AAP (1944) Spreading depression of activity in the cerebral cortex. *J Physiol* 7: 359–390.
7. Grafstein B (1956) Mechanism of spreading cortical depression. *J Neurophysiol* 19:154–171.
8. Gardner-Medwin AR (1981) Possible roles of vertebrate neuroglia in potassium dynamics, spreading depression and migraine. *J Exp Biol* 95:111–127.
9. Somjen GG (2001) Mechanisms of spreading depression and hypoxic spreading depression-like depolarization. *Physiol Rev* 81:1065–1096.
10. Charles A, Brennan K (2009) Cortical spreading depression: New insights and persistent questions. *Cephalalgia* 29:1115–1124.
11. Pietrobon D, Moskowitz MA (2014) Chaos and commotion in the wake of cortical spreading depression and spreading depolarizations. *Nat Rev Neurosci* 15:379–393.
12. Ransom CB, Ransom BR, Sontheimer H (2000) Activity-dependent extracellular K+ accumulation in rat optic nerve: The role of glial and axonal Na+ pumps. *J Physiol* 522:427–442.
13. Kofuji P, Newman EA (2004) Potassium buffering in the central nervous system. *Neuroscience* 129:1045–1056.
14. Wang F, et al. (2012) Astrocytes modulate neural network activity by Ca^2+-dependent uptake of extracellular K+. *Sci Signal* 5:ra26.

15. Nedergaard M, Hansen AJ (1988) Spreading depression is not associated with neuronal injury in the normal brain. *Brain Res* 449:395–398.
16. Yanamoto H, et al. (2004) Spreading depression induces long-lasting brain protection against infarcted lesion development via BDNF gene-dependent mechanism. *Brain Res* 1019:178–188.
17. Nedergaard M, Astrup J (1986) Infarct rim: Effect of hyperglycemia on direct current potential and [^{14}C]2-deoxyglucose phosphorylation. *J Cereb Blood Flow Metab* 6: 607–615.
18. Lauritzen M, et al. (2011) Clinical relevance of cortical spreading depression in neurological disorders: Migraine, malignant stroke, subarachnoid and intracranial hemorrhage, and traumatic brain injury. *J Cereb Blood Flow Metab* 31:17–35.
19. Dreier JP (2011) The role of spreading depression, spreading depolarization and spreading ischemia in neurological disease. *Nat Med* 17:439–447.
20. Iliff JJ, et al. (2012) A paravascular pathway facilitates CSF flow through the brain parenchyma and the clearance of interstitial solutes, including amyloid β. *Sci Transl Med* 4:147ra111.
21. Xie L, et al. (2013) Sleep drives metabolite clearance from the adult brain. *Science* 342: 373–377.
22. Cotrina ML, Lou N, Tome-Garcia J, Goldman J, Nedergaard M (2017) Direct comparison of microglial dynamics and inflammatory profile in photothrombotic and arterial occlusion evoked stroke. *Neuroscience* 343:483–494.
23. Li X, et al. (2004) Chronic behavioral testing after focal ischemia in the mouse: Functional recovery and the effects of gender. *Exp Neurol* 187:94–104.
24. Kerr JND, Greenberg D, Helmchen F (2005) Imaging input and output of neocortical networks in vivo. *Proc Natl Acad Sci USA* 102:14063–14068.
25. Frydenlund DS, et al. (2006) Temporary loss of perivascular aquaporin-4 in neocortex after transient middle cerebral artery occlusion in mice. *Proc Natl Acad Sci USA* 103: 13532–13536.
26. Kiening KL, et al. (2002) Decreased hemispheric Aquaporin-4 is linked to evolving brain edema following controlled cortical impact injury in rats. *Neurosci Lett* 324: 105–108.
27. Yeh T-H, et al. (2005) Glutamate transporter function of rat hippocampal astrocytes is impaired following the global ischemia. *Neurobiol Dis* 18:476–483.
28. Wang M, et al. (2012) Cognitive deficits and delayed neuronal loss in a mouse model of multiple microinfarcts. *J Neurosci* 32:17948–17960.
29. Igarashi H, Huber VJ, Tsujita M, Nakada T (2011) Pretreatment with a novel aquaporin 4 inhibitor, TGN-020, significantly reduces ischemic cerebral edema. *Neurol Sci* 32: 113–116.
30. Manley GT, et al. (2000) Aquaporin-4 deletion in mice reduces brain edema after acute water intoxication and ischemic stroke. *Nat Med* 6:159–163.
31. Manley GT, Binder DK, Papadopoulos MC, Verkman AS (2004) New insights into water transport and edema in the central nervous system from phenotype analysis of aquaporin-4 null mice. *Neuroscience* 129:983–991.
32. Amiry-Moghaddam M, et al. (2003) An alpha-syntrophin-dependent pool of AQP4 in astroglial end-feet confers bidirectional water flow between blood and brain. *Proc Natl Acad Sci USA* 100:2106–2111.
33. Ikeshima-Kataoka H, Abe Y, Abe T, Yasui M (2013) Immunological function of aquaporin-4 in stab-wounded mouse brain in concert with a pro-inflammatory cytokine inducer, osteopontin. *Mol Cell Neurosci* 56:65–75.
34. Arakawa S, Nakamura S, Kawashima N, Nishiike S, Fujii Y (1997) Antidromic burst activity of locus coeruleus neurons during cortical spreading depression. *Neuroscience* 78:1147–1158.
35. Ding S, Wang T, Cui W, Haydon PG (2009) Photothrombosis ischemia stimulates a sustained astrocytic Ca2+ signaling in vivo. *Glia* 57:767–776.
36. Ding F, et al. (2013) α1-Adrenergic receptors mediate coordinated Ca2+ signaling of cortical astrocytes in awake, behaving mice. *Cell Calcium* 54:387–394.
37. Paukert M, et al. (2014) Norepinephrine controls astroglial responsiveness to local circuit activity. *Neuron* 82:1263–1270.
38. Globus MY-T, et al. (1989) Direct evidence for acute and massive norepinephrine release in the hippocampus during transient ischemia. *J Cereb Blood Flow Metab* 9: 892–896.
39. Ding F, et al. (2016) Changes in the composition of brain interstitial ions control the sleep-wake cycle. *Science* 352:550–555.
40. Schain AJ, Melo-Carrillo A, Strassman AM, Burstein R (2017) Cortical spreading depression closes paravascular space and impairs glymphatic flow: Implications for migraine headache. *J Neurosci* 37:2904–2915.
41. Hirt L, et al. (2017) Improved long-term outcome after transient cerebral ischemia in aquaporin-4 knockout mice. *J Cereb Blood Flow Metab* 37:277–290.
42. Shi W-Z, et al. (2012) Aggravated inflammation and increased expression of cysteinyl leukotriene receptors in the brain after focal cerebral ischemia in AQP4-deficient mice. *Neurosci Bull* 28:680–692.
43. Zeng X-N, et al. (2012) AQP4 knockout aggravates ischemia/reperfusion injury in mice. *CNS Neurosci Ther* 18:388–394.
44. Padmawar P, Yao X, Bloch O, Manley GT, Verkman AS (2005) K+ waves in brain cortex visualized using a long-wavelength K+-sensing fluorescent indicator. *Nat Methods* 2: 825–827.
45. Binder DK, et al. (2006) Increased seizure duration and slowed potassium kinetics in mice lacking aquaporin-4 water channels. *Glia* 53:631–636.
46. Haj-Yasein NN, et al. (2015) Deletion of aquaporin-4 increases extracellular K(+) concentration during synaptic stimulation in mouse hippocampus. *Brain Struct Funct* 220:2469–2474.
47. Mulligan SJ, MacVicar BA (2004) Calcium transients in astrocyte endfeet cause cerebrovascular constrictions. *Nature* 431:195–199.
48. Bekar LK, He W, Nedergaard M (2008) Locus coeruleus alpha-adrenergic-mediated activation of cortical astrocytes in vivo. *Cereb Cortex* 18:2789–2795.
49. Kuhmonen J, et al. (1997) Neuroprotective effects of dexmedetomidine in the gerbil hippocampus after transient global ischemia. *Anesthesiology* 87:371–377.
50. Jolkkonen J, et al. (1999) Neuroprotection by the α2-adrenoceptor agonist, dexmedetomidine, in rat focal cerebral ischemia. *Eur J Pharmacol* 372:31–36.
51. Brede M, et al. (2011) α(2)-Adrenoceptors do not mediate neuroprotection in acute ischemic stroke in mice. *J Cereb Blood Flow Metab* 31:e1–e7.
52. Kuhmonen J, Haapalinna A, Sivenius J (2001) Effects of dexmedetomidine after transient and permanent occlusion of the middle cerebral artery in the rat. *J Neural Transm (Vienna)* 108:261–271.
53. Jolkkonen J, et al. (2000) Behavioral effects of the α(2)-adrenoceptor antagonist, atipamezole, after focal cerebral ischemia in rats. *Eur J Pharmacol* 400:211–219.
54. Karhunen H, Virtanen T, Schallert T, Sivenius J, Jolkkonen J (2003) Forelimb use after focal cerebral ischemia in rats treated with an α 2-adrenoceptor antagonist. *Pharmacol Biochem Behav* 74:663–669.
55. Puurunen K, Jolkkonen J, Sirviö J, Haapalinna A, Sivenius J (2001) An α(2)-adrenergic antagonist, atipamezole, facilitates behavioral recovery after focal cerebral ischemia in rats. *Neuropharmacology* 40:597–606.
56. Butovas S, Lukkarinen J, Virtanen T, Jolkkonen J, Sivenius J (2001) Differential effect of the alpha2-adrenoceptor antagonist, atipamezole, in limb-placing task and skilled forepaw use following experimental stroke. *Restor Neurol Neurosci* 18:143–151.
57. Beltran EJ, Papadopoulos CM, Tsai S-Y, Kartje GL, Wolf WA (2010) Long-term motor improvement after stroke is enhanced by short-term treatment with the alpha-2 antagonist, atipamezole. *Brain Res* 1346:174–182.
58. Barbelivien A, Jolkkonen J, Rutkauskaite E, Sirviö J, Sivenius J (2002) Differentially altered cerebral metabolism in ischemic rats by α2-adrenoceptor blockade and its relation to improved limb-placing reactions. *Neuropharmacology* 42:117–126.
59. Dennis T, L'Heureux R, Carter C, Scatton B (1987) Presynaptic alpha-2 adrenoceptors play a major role in the effects of idazoxan on cortical noradrenaline release (as measured by in vivo dialysis) in the rat. *J Pharmacol Exp Ther* 241:642–649.
60. Abercrombie ED, Keller RW, Jr, Zigmond MJ (1988) Characterization of hippocampal norepinephrine release as measured by microdialysis perfusion: Pharmacological and behavioral studies. *Neuroscience* 27:897–904.
61. Monai H, et al. (2016) Calcium imaging reveals glial involvement in transcranial direct current stimulation-induced plasticity in mouse brain. *Nat Commun* 7:11100.
62. Hira R, et al. (2014) Reward-timing-dependent bidirectional modulation of cortical microcircuits during optical single-neuron operant conditioning. *Nat Commun* 5:5551.
63. Brenner M, Kisseberth WC, Su Y, Besnard F, Messing A (1994) GFAP promoter directs astrocyte-specific expression in transgenic mice. *J Neurosci* 14:1030–1037.
64. Takata N, et al. (2013) Cerebral blood flow modulation by Basal forebrain or whisker stimulation can occur independently of large cytosolic Ca2+ signaling in astrocytes. *PLoS One* 8:e66525.
65. McBride DW, Klebe D, Tang J, Zhang JH (2015) Correcting for brain swelling's effects on infarct volume calculation after middle cerebral artery occlusion in rats. *Transl Stroke Res* 6:323–338.
66. Swanson RA, et al. (1990) A semiautomated method for measuring brain infarct volume. *J Cereb Blood Flow Metab* 10:290–293.